

We are IntechOpen, the world's leading publisher of Open Access books Built by scientists, for scientists

6,900

Open access books available

186,000

International authors and editors

200M

Downloads

Our authors are among the

154

Countries delivered to

TOP 1%

most cited scientists

12.2%

Contributors from top 500 universities



WEB OF SCIENCE™

Selection of our books indexed in the Book Citation Index
in Web of Science™ Core Collection (BKCI)

Interested in publishing with us?
Contact book.department@intechopen.com

Numbers displayed above are based on latest data collected.
For more information visit www.intechopen.com



A Contribution to the Reduction of Radiometric Miscalibration of Pushbroom Sensors

Christian Rogaß* et al.**

*Helmholtz Centre Potsdam, GFZ German Research Centre for Geosciences,
Germany*

1. Introduction

Imaging spectroscopy is used for a variety of applications such as the identification of surface cover materials and its spatiotemporal monitoring. Contrary to multispectral instruments more spectral information can be incorporated in the differentiation of materials. New generations of sensors are based on the pushbroom technology, where a linear array of sensors perpendicular to the flight direction scans the full width of the collected data in parallel as the platform moves. Contrary to whiskbroom scanners that collect data one pixel at a time pushbroom systems can simply gather more light as they sense a particular area for a longer time. This leads to a better Signal-to-Noise Ratio (SNR). In addition, the two dimensional photo detector array in pushbroom systems may enable different readout configuration settings, such as spatial and/or spectral binning, allowing a better control of the SNR. It follows from this that low reflective materials can be potentially sensed as well as high reflective materials without saturating the detector elements. However, the use of detector arrays requires a precise radiometric calibration as different detectors might have different physical characteristics. Any miscalibration results in visually perceptible striping and uncertainties increase in preceding analyses such as classification and segmentation (Datt et al., 2003). There are various reasons for miscalibration, for instance temporal fluctuations of the sensor temperature, deprecated calibration coefficients or uncertainties in the modelling of the calibration coefficients. In addition, ageing and environmental stresses highly affect the mechanical and optical components of a sensor system; its reliability is thus not such to grant unchanged calibration accuracies for the entire mission life span.

Radiometric calibration and the estimation of the calibration coefficients can be considered as the assignment of known incident at-sensor radiance to measured digital numbers (DN). For this, physically known, different reflective targets are artificially illuminated by electromagnetic radiation of a specific spectrum and the reflected radiation is then recorded by the sensor that consists of a number of detectors. Then, the response of each detector is

* Corresponding Author

** Daniel Spengler¹, Mathias Bochow¹, Karl Segl¹, Angela Lausch², Daniel Doktor², Sigrid Roessner¹, Robert Behling¹, Hans-Ulrich Wetzel¹, Katia Urata¹, Andreas Hueni³ and Hermann Kaufmann¹

¹Helmholtz Centre Potsdam, GFZ German Research Centre for Geosciences, Germany

²Helmholtz Centre for Environmental Research, UFZ Germany

³Remote Sensing Laboratories, University of Zurich, Switzerland

modelled with respect to the incident radiation, the reflective target and the defined illumination of the target. The mathematical modelling is often performed by applying a linear least squares regression. Contemporary, differences of detectors are balanced.

Consequently, calibration coefficients are obtained – shortly named as offset and slope. Offsets incorporate the unwanted detector-dependent dark current that is caused by thermally generated electrons (Oppelt and Mauser, 2007). In turn, slopes directly relate radiance to DN. Offsets are often measured before any image acquisition, but may change due to instabilities in the cooling system. Mechanical stress or uncertainties in foregoing laboratory calibration can cause changes in the physical characteristics of detectors as well. In order to support laboratory calibration, in-flight calibrations complement the calibration procedure, verifying the results obtained in the laboratory and, in addition, allowing the measurement of parameters that are only obtainable during flight (i.e. stability measurements, solar calibration, etc).

For this, physically known targets have to be sensed and incident illumination should be measured during the overflight. Uncertainties in the measurement of hemispheric incident solar radiation and in the incorporation of illumination, sensing and wavelength dependent response of imaged calibrations targets on incident light aggravate then this type of calibration and may also lead to miscalibrations or visually perceptible image stripes. Hence, any striping reduction or retrieval of calibration coefficients should reduce stripes and at the same time the spectral characteristics of the imaged surface materials have to be preserved.

In the literature, specific approaches for destriping of slope stripes, offset stripes or both exist, and these are primarily based on methods such as interpolation (Oliveira and Gomes, 2010; Tsai and Chen, 2008), local or global image moments (Datt et al., 2003; Cavalli et al., 2008; Le Maire et al., 2008; Liu et al., 2009), filtering (Garcia and Moreno, 2004; Shen et al., 2008; Simpson et al., 1995, Simpson et al., 1998) or complex image statistics of log transformed slopes (Bouali and Ladjal, 2010; Carfantan and Idier, 2010; Gomez-Chova et al., 2008). Most methods replace original, miscalibrated radiances. This should be only applied if information is completely missing or erroneous.

In the following, a framework that efficiently reduces linear as well as nonlinear miscalibration is reviewed concurrently preserving the spectral characteristics of sensed surface cover materials. This framework, originally proposed by Rogass et al. (2011) and named as Reduction of Miscalibration Effects (ROME), consists of a linear and a nonlinear slope reduction and an offset reduction that are consecutively performed and does not require a priori information or scene and sensor specific parameterisation.

Before any radiometric miscalibration reduction is applied, image gradients that are not orthogonal to the image are excluded if they do not represent the image content. Here, Minkowski metrics, gradient operators and edge extraction algorithms are combined to exclude discontinuities if they do not dominate the image content (Canny, 1986; Haralick et al., 1987; Rogass et al., 2009). The linear and the nonlinear slope reduction of ROME are performed for each detector element and band without any information from other detector elements. The offset reduction of ROME considers adjacent image columns and refers to a predefined image column (first column per default) that is assumed to be the reference. Specific image quality metrics, such as the change in SNR (Gao, 1993; Atkinson et al., 2005), were used to evaluate the necessity of such preceding reduction.

After these preceding reductions the image is radiometrically band wise rescaled to recover the radiometric scale. This is necessary since uncertainties in the estimation of parameters (e.g., detector resolution in the linear slope reduction) and in the incorporation of miscalibrated reference areas (e.g., potential miscalibration of the first image column as reference for the offset reduction) remain. The rescaling of ROME assumes that image columns that were less corrected than others can be used as reference for the whole image. After all reductions a detrending is performed reducing across track brightness gradients caused by reduction related frequency undershoots of low SNR bands. In this work an extension of ROME's detrend approach is presented evidencing an effective reduction of undershoots when compared to the original approach.

In order to test the robustness of the algorithm due to different types of miscalibration, four grey valued images as well as 12 multispectral and hyperspectral scenes were considered. The grey valued images were randomly striped by linearly varying slope and/or offset. One HyMAP scene was three times differently and artificially striped by offset stripes. The simulated EnMAP scene was not corrected for nonlinear effects and, hence, the nonlinear correction facilities were tested. Miscalibrated scenes acquired by AISA DUAL (3 scenes), Hyperion (2 scenes), ASTER (1 scene), CHRIS/Proba (1 scene) and APEX (1 scene) were additionally processed.

2. Materials

In Rogass et al. (2011) four grey valued images (Fig. 1) from the image database of the Signal and Image Processing Institute (SIPI) of the University of California (Weber, 1997), 512×512 pixels in size, and six hyperspectral scenes (3 AISA DUAL, 2 Hyperion and 1 EnMAP) were selected to test and to evaluate the performance of the proposed ROME framework. The grey valued samples as well as the EnMAP scene were considered as noise free. However, the 'Lenna' image (Fig. 1a) and the 'Mandrill' image (Fig. 1b) are excluded from further considerations due to their unique spectral and spatial properties as detailed described in Rogass et al. (2011).

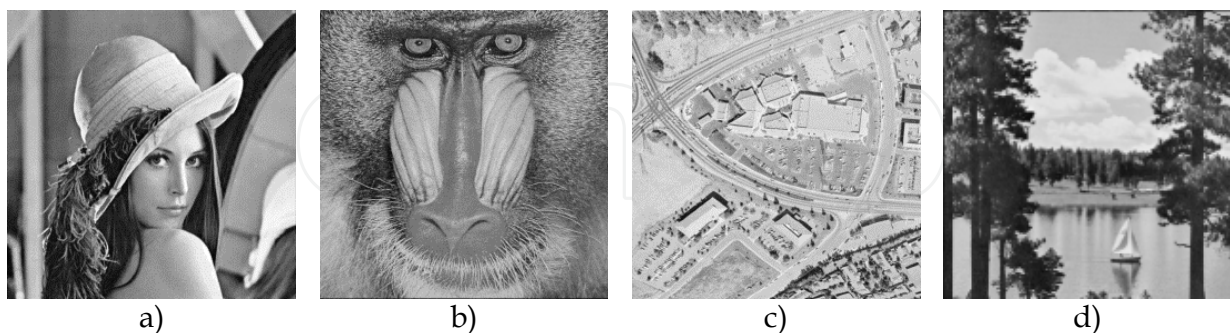


Fig. 1. Grey scaled image samples from the USC SIPI image data base considered in the following as a) 'Lenna', b) 'Mandrill', c) 'Aerial' and d) 'Sailboat on lake'

To simulate different types of miscalibrations and to evaluate their impact on the proposed work, the two grey valued images (Fig. 1 c and d) and the EnMAP scene were artificially degraded. The grey valued images were randomly degraded by applying 800 different sets of multiplicative (slope) and/or additive (offset) Gaussian white noise (Box and Muller,

1958). These 800 noisy matrices were transformed to provide always a mean equal to zero and standard deviations ranging from 0.0001 to 10000 for the multiplicative parts and from -10000 to 10000 for the additive part. Such high noise levels were chosen to also simulate low SNR scenarios that are noise dominated. More details on the noise matrices and the hyperspectral scenes are given in Rogass et al. (2011).

In this work additional scenes from APEX, ASTER and CHRIS/Proba were inspected, destriped and evaluated. Contemporary, one HyMAP scene was selected and three times artificially and additively degraded by Gaussian white noise to extend the testing of correction facilities for airborne sensors. After degrading three mean SNR levels of 7.6, 76 and 760 were simulated.

The HyMAP sensor is a hyperspectral whiskbroom airborne sensor that consists of one detector column and, hence, offset miscalibrations cannot be perceived as image stripes since each image column has the same offset. Therefore, HyMAP image acquisitions can be used to test correction approaches for pushbroom sensors.

In the following, an image column or across track is considered as x and an image row or along track is considered as y .

3. Methods

3.1 Calibration basics

Radiometric calibrations are often performed in laboratory and basically assign known incident at-sensor radiance to measured digital number (DN). The association is usually realised by a linear least squares regression that minimises the difference between modelled at-sensor radiance and known at-sensor radiance. The regression coefficients are also used in the reverse process to assign measured DN to at-sensor radiance that is considered as radiometric scaling (Chander et al., 2009).

However, uncertainties in the laboratory measurements, in the mathematical modelling and in the incorporation of temporal changes of the detector characteristics lead to miscalibrations and, hence, to visually perceptible image stripes in y -direction. In the following it will be exemplarily shown how to suppress miscalibrations in accordance with the ROME framework. This framework consists of multiple steps that are consecutively processed (Fig. 2).



Fig. 2. Workflow of ROME destriping per band

Pushbroom sensors have detector arrays. Each detector pixel of the array has different physical characteristics. It follows from this that an uncalibrated hyperspectral image is striped. The radiometric calibration and the reverse process - radiometric scaling - aim at the assignment of incident radiance to DN and vice versa. Usually, radiometric calibration can be performed in-flight, vicariously (Biggar et al., 2003; Bruegge et al., 2007), over a flat field (Bindschadler and Choi, 2003) or in laboratory.

In the process of calibration each detector of the detector array must be solely considered. Known incident radiation reaches a detector pixel and once the incident photons have sufficient energy to excite electrons into a certain energy level, electron-hole pairs are generated – a phenomenon that is known as the photoelectric effect. These free charges are then transmitted and read out through sensor electronic. Dispersive optics placed in front of the sensor disperses the incident radiation into different wavelengths that is further projected into each row of the detector array. The physical response, considered as signal S in electrons, of one detector element of a pushbroom sensor to incident radiation L can be approximated by a nonlinear relation (Dell'Endice, 2008; Dell'Endice et al., 2009):

$$S(e^-) \propto \frac{F \cdot L \cdot A \cdot \tan^2\left(\frac{\text{FOV}}{2}\right) \cdot \tau \cdot T \cdot \lambda \cdot \eta \cdot \text{SSI}}{h \cdot c \cdot n_e^2} \quad (1)$$

where L is the at-sensor-radiance, A is the optical aperture of the sensing instrument, FOV is the field of view, T is the integration time, SSI is the Spectral Sampling Interval in respect to the Full Width at Half Maxima, h is the Planck constant, c is the speed of light, n_e is the number of collected electrons, τ is the optical transmission, λ is the centre wavelength, η is the quantum efficiency and F is the filter efficiency. This can be then related to the recorded digital number DN as follows:

$$\text{DN} = \frac{(S + N) \cdot \text{DN}_{\max}}{\text{FWC}} + \text{DN}_0 \quad \wedge \quad S \leq \text{FWC} \quad (2)$$

where N is a noise term incorporating Shot-Noise, read-out noise and dark noise, DN_{\max} is the radiometric resolution, FWC is the Full Well Capacity that defines the detector saturation and DN_0 is the dark current. To enable a mathematical modelling relating incident radiation and measured DN , either the illumination is changed in a defined way or the integration time is changed or targets of different reflective properties are sensed. The association of at-sensor radiance L to DN is broadly considered as radiometric calibration or, reversely, as radiometric scaling (Chander et al., 2009). To reduce the influence of noise, a specific number of measurements is required. Then, the association can be realised, e.g., by least squares polynomial fit that minimises the differences between modelled and measured at-sensor radiance (Barducci et al., 2004; Xiong and Barnes, 2006). The minimisation of the merit function gives then the transformation coefficients for the association. This can be achieved by applying the following model:

$$\chi^2 = \sum_{j=1}^{N_{\text{targets}}} \left[L - \left(c_0 + \sum_{i=1}^M c_i \cdot \text{DN}^i \right) \right]^2 \quad \wedge \quad M \geq 1; N_{\text{targets}} \geq 2 \quad (3)$$

where N_{targets} denotes the number of calibration targets, c_0 is the offset regarding the dark current, and M is the polynomial degree. The more the detector response differ from a linear response, the more it is necessary to use a polynomial degree higher as one. Mostly, detector responses can be mathematically modelled. Potential changes in the characteristics of detectors require frequent calibrations that are not practicable.

However, if then along track stripes in radiometrically scaled images are perceptible miscalibration is indicated. In that case, it is necessary to determine the type of miscalibration – multiplicative or additive – linear or nonlinear. In ROME this is performed by comparing the output SNR to the input SNR due to the specific processing step (Brunn et al., 2003; Gao, 1993). If the SNR is increased, a successful operation is indicated and finally applied. In the following the stripe types are distinguished with respect to equation 3 – additive c_0 and multiplicative $c_{1,M}$ miscalibration and reduction. In any case the reduction of miscalibration should be applied before rectification.

3.2 Edge exclusion

Discontinuities such as impulse noise, edges or translucent objects like tree vegetation should be excluded from further processing unless they contribute a high spatial distribution. This is relevant for approaches that aim on the reduction of miscalibration by relying on statistical analyses of spatial and spectral differences in homogeneous regions. Edges can be generally excluded if they do not coincide with along track or across track direction. Since uncertainties in the impact of edges on the reduction process remain edges should be excluded if they do not dominate image content (compare Fig. 1b). In ROME this is performed by a combination of edge detection algorithms with morphological dilation with respect to Minkowski metrics. Potential edge detection algorithms for single banded images must be then adapted to incorporate only along track gradients, because gradients of radiometric miscalibration might superimpose across track gradients. In Rogass et al. (2011) the Canny algorithm (Canny, 1986) is used for single banded images and the Hyperspectral Edge Detection Algorithm (HEDA) is used for multi banded images (Rogass et al., 2010). After obtaining binary edge maps morphological dilations (Haralick et al., 1987; Rogass et al., 2009) are additionally applied to minimise edge adjacency effects caused by Point Spread Function (PSF) related blooming of edges into adjacent regions. The reversed edge map gives then the mask. In case of tree vegetation indices are computed and pixel wise thresholded by the highest two likelihood quartiles of containing vegetation. This binary vegetation map is reversed and multiplied with the reversed binary edge map. Hence, edges and translucent vegetation is excluded. Related equations are given in Rogass et al. (2010) and Rogass et al. (2011). The application of the reverse edge map gives then an edge filtered image.

3.3 Linear c_1 slope reduction

In case of linear miscalibration each pixel of one detector (one column) of the same channel is scaled by the same c_1 slope (the term ‘gain’ is often misleading used and corresponds to the maximisation of the radiometric resolution; Chander et al., 2009). A simple differential operation between two pixels from the same column leads to the mathematical elimination of the c_0 offset. This difference is then equivalent to the difference of radiance levels. This corresponds to the c_1 slope of this detector times the spectral difference of surface cover materials constrained by the detector resolution. Hence, a reduction of c_1 miscalibration must recover both c_1 slope and the spectral characteristics of the surface cover material. In ROME this is performed per detector or column and band by applying a multistep approach. Here, the radiances are sorted in ascending order. Then, unique radiance values are extracted and ascendingly sorted. Next, all adjacent differences are extracted, i.e. the

second unique value is subtracted from the first one, the third unique value from the second one and so on. Then, the probability distribution of these differences is estimated by a histogram. The first frequency category (first bin) contains the smallest difference of unique values. The smallest difference is given as the minimum of all differences of this bin and represents the slope times the smallest difference of unique values (SDUV) of a perfectly calibrated band. The SDUV can be considered equivalent to the spectral detector resolution of the considered band. To estimate the slope, it is now necessary to assess the SDUV. This can be straightforwardly performed by computing the median of all binned differences. After dividing this smallest difference by the SDUV the slope for this band and detector is recovered. This is performed for each band and detector. After obtaining the slope coefficients the applicability is validated. This is performed by considering adjacent detector columns. For this, the shapes of the histograms of adjacent columns are inspected. If the number of frequency categories and the positions of the maxima are not equal, then the slope reduction is applied for the considered column. This evaluation bases on the assumption that significant different slopes of similar and adjacent detectors cause stretches (broadening) and shifts in the histogram since considered columns mostly cover the same regions and the related point spread functions (PSF) of each detector are stable during image acquisition and, hence, contribute to their neighbouring pixels the same fraction of their center pixel. In presence of c_0 offset miscalibration these offsets are reduced concurrently to c_0/c_1 . Subsequently, SNR is computed to indicate whether previous operation is necessary or not. However, radiometric rescaling is then applied to reduce uncertainties in the estimation of SDUV (see section 3.5).

3.4 Linear c_0 reduction

In the following it is assumed that the thermally induced offset is constant during one image acquisition and that homogeneous regions are spectrally homogeneous. It follows from this that the offset of one detector element and wavelength contributes the same fraction to all pixels of one detector column and wavelength. Hence, spectral homogeneous regions that appear spectrally different indicate c_0 miscalibration if linear c_1 or nonlinear $c_{2..M}$ reductions were performed beforehand. To reduce c_0 miscalibration, it is necessary to spectrally compare adjacent image columns and to relate succeeding reduction to a predefined column (ROME uses per default the first column). In ROME the differences between adjacent columns are computed and binned in a histogram. Then, it is assumed that the bin (frequency category) with the highest frequency most likely contain the offset difference. To finally assess the offset difference, it is only necessary to average the differences of each bin by the median, to weight the bin according its frequency and to sum all weighted and averaged differences. After c_0 reduction a radiometric rescaling should be applied as in ROME to avoid erroneous radiometric levelling due to the used reference column. However, after applying an offset reduction, it is necessary to check whether this operation was necessary or not. In ROME this is performed by considering the evolution of the SNR.

3.5 Radiometric rescaling

Previous described approaches to correct data for miscalibration can change the mean radiation of a band that is only acceptable if the new mean is closer to a perfect calibrated band compared to the mean of the uncorrected band. This is not known yet and, hence, it is

necessary to recover the physical meaning of such. A simple rescaling to the old maximum and minimum cannot be applied since it can be assumed that the old maximum and minimum are biased or erroneous due to miscalibration. In order to preserve the spectral characteristics a specific approach was proposed within the ROME framework as detection of lowest reduction zones. In this approach the correction vectors are inspected in a moving window. In each window the mean of the first and last reduction is rationed by the middle window reduction. After computing all windowed ratios the ratio that is closest to one is selected as reference. Then, the middle column of the reference is considered with regard to its maximum and minimum. The old maximum and minimum, i.e. before any reduction, is compared with the extrema of the reference. These are used to obtain linear transformation coefficients for the whole band that are subsequently applied.

3.6 Extended detrending

In Rogass, et al. (2011) a detrending approach is proposed that aims on the reduction of across track brightness gradients that are caused by offset reduction related frequency undershoots or by material, illumination and viewing geometry dependent surface responses on incident light. These undershoots have a medium frequency on average in comparison to the spatial distribution of the image content.

In ROME the detrending is realised per band by computing the median average of each column, by smoothing and mean normalising this column to its related average vector and by applying this vector on the image by row wise division.

However, lower frequencies are not considered in ROME as they can be perceived as broad brightness gradients. In this work, the new detrending approach is extended to capture lower frequency undershoots. For this, the column median per band of the uncorrected image and the corrected image is computed. This then gives one vector per band and image of the same length as the number of detectors. Each vector is then fitted to a second order polynomial with regard to least squares principles. Consequently, polynomial coefficients for each vector and image are obtained. The polynomial coefficients of the uncorrected image are subtracted from the coefficients of the corrected image. This gives differential coefficients for each band of the corrected image. After this an index vector is created that contains the same number of elements as detectors and consists of detector numbers (i.e. 0, 1, 2, 3... etc.). This could be considered as a x-vector. The x-vector is used to obtain functional values of the differential polynomials. This then gives the differential low frequency trend of this band with respect to the corrected and the uncorrected image. This trend is applied contrary to the detrending of ROME by row wise addition. Both the original detrending of ROME and this extension of the detrending enable a correction for medium and low frequency undershoots. A comparison of this approach and the originally proposed approach of ROME will be given in the results chapter.

3.7 Image quality metrics

In Rogass et al. (2011) several image quality metrics were combined to evaluate destriping results on the one hand and to avoid potential drawbacks associated with relying on a single type of evaluation on the other hand. In this work the same metrics are used. Those were the global Peak-Signal-to-Noise-Ratio (PSNR) (Rogass et al., 2010; Wang and Bovik, 2009), the

global Shannon Entropy (Rogass et al., 2010, Frank and Smith, 2010) and the local Modified Structural Similarity Index (MSSIM) (Tsai and Chen, 2008; Wang and Bovik, 2009, Wang et al., 2004). In case of available ground truth as for the HyMAP scene the metrics were applied on the result and on ground truth. In case of missing ground truth the metrics were applied on both the input and the output, but can only be relatively considered.

4. Results and discussion

The ROME framework is the most recent approach to recover radiometric calibration in presence of miscalibration. In this work more tests were included to show that ROME is able to reduce miscalibration of broadly used sensors. The summarised results of Tab. 1 show how miscalibration was reduced that is detailed discussed per newly considered sensor in the next sections. All newly tested sensors were miscalibrated due to varying dark current.

Sensor	Scene	PSNR	Entropy	MSSIM	Average
APEX	1	4 %	19 %	1 %	8 %
ASTER	1	4 %	19 %	1 %	8 %
CHRIS	1	1 %	0 %	3 %	1 %
HyMAP	SNR=7.6	-5 %	4%	6 %	5 %
	SNR=76	0 %	3 %	5 %	3 %
	SNR=760	0 %	2 %	5 %	2 %
AISA ^{1,2}	1	-2 %	9 %	8 %	5 %
EnMAP ^{1,2}	1	2 %	8 %	7%	6 %
Grey images ^{1,2}	3,4	4 %	4 %	2 %	3 %
Hyperion ^{1,2}	1	2 %	5 %	7 %	5 %

¹ compared to ground truth; ² from Rogass et al. (2011)

Table 1. Destriping results

4.1 Grey valued images

The grey valued images that have been selected for testing in Rogass et al. (2011) cover a broad range of spectral and spatial image properties. In this work 2 out of 4 of the test images were selected due to their similar spatial and spectral distributions compared to remote sensing scenes. The ‘Aerial’ image is characterised by leptokurtic grey value distribution. The ‘Sailboat on lake’ image has a balanced grey value distribution and edge quantity. With regard to Rogass et al. (2011) ROME achieved a destriping accuracy of 97 % (compare Tab. 1 and Fig. 3) for the two grey test images. As perceptible in Fig. 3 all stripes were removed and the results differ from ground truth (Fig. 1c and d) only by 3% on average (Tab. 1).

4.2 Artificial striped HyMAP

The HyMAP whiskbroom sensor was three times differently offset striped, ROME destriped and the results were evaluated based on the metrics of section 3.7. The offset stripes were

generated as described in Rogass et al. (2011) and scaled to achieve an overall SNR of 7.6, 76 and 760. The offset stripe type was selected since this type is most common to broadly used pushbroom sensors. However, about 97 % of a perfect calibration could be recovered (compare Tab. 1). Hence, the accuracy assumption of Rogass et al. (2011) that 97 % of a perfect calibration can be recovered by ROME is confirmed. With regard to the results visually presented in Fig. 4 the stripes were completely removed.

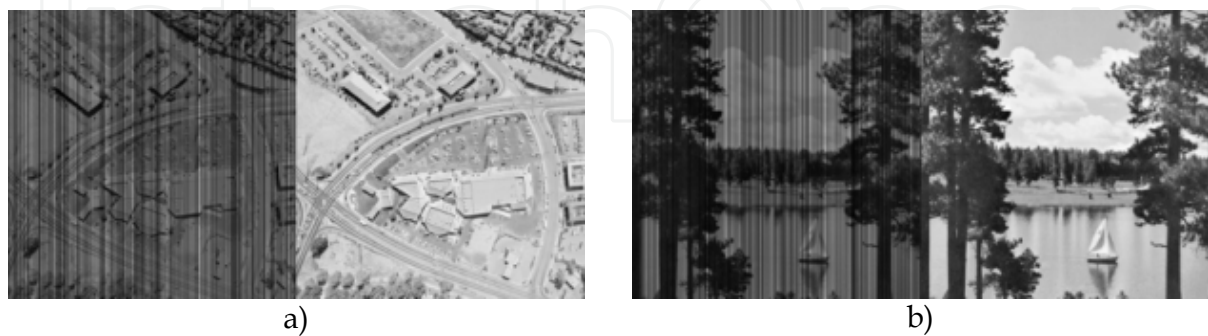


Fig. 3. Striped (left) and destriped images (right) for a) ‘Aerial’ and b) ‘Sailboat on lake’

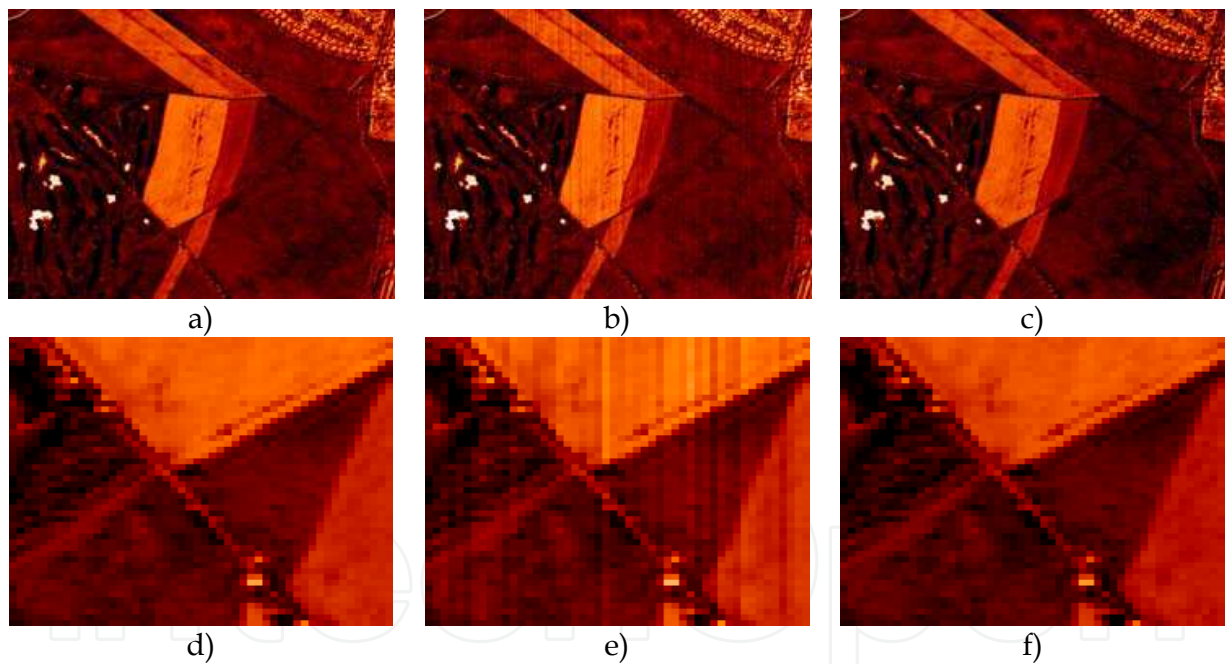


Fig. 4. False coloured image subset of band 30 (874 nm) of a HyMAP scene (subset a and zoom d), striped representation with a SNR of 7.6 (subset b and zoom e) and the ROME result adaptively detrended (subset c and zoom f)

Uncertainties remain in the assessment of the true radiometric scale as well as in the correct trend. This is visualised in Fig. 5. Considering both the transect and the spectral profile of Fig. 5 leads to the perception that small differences between ground truth and the destriping result persist. These differences approximately amounts 3% due to Tab. 1. This underlines the robustness of the ROME approach and contemporary shows that miscalibration can be efficiently suppressed.

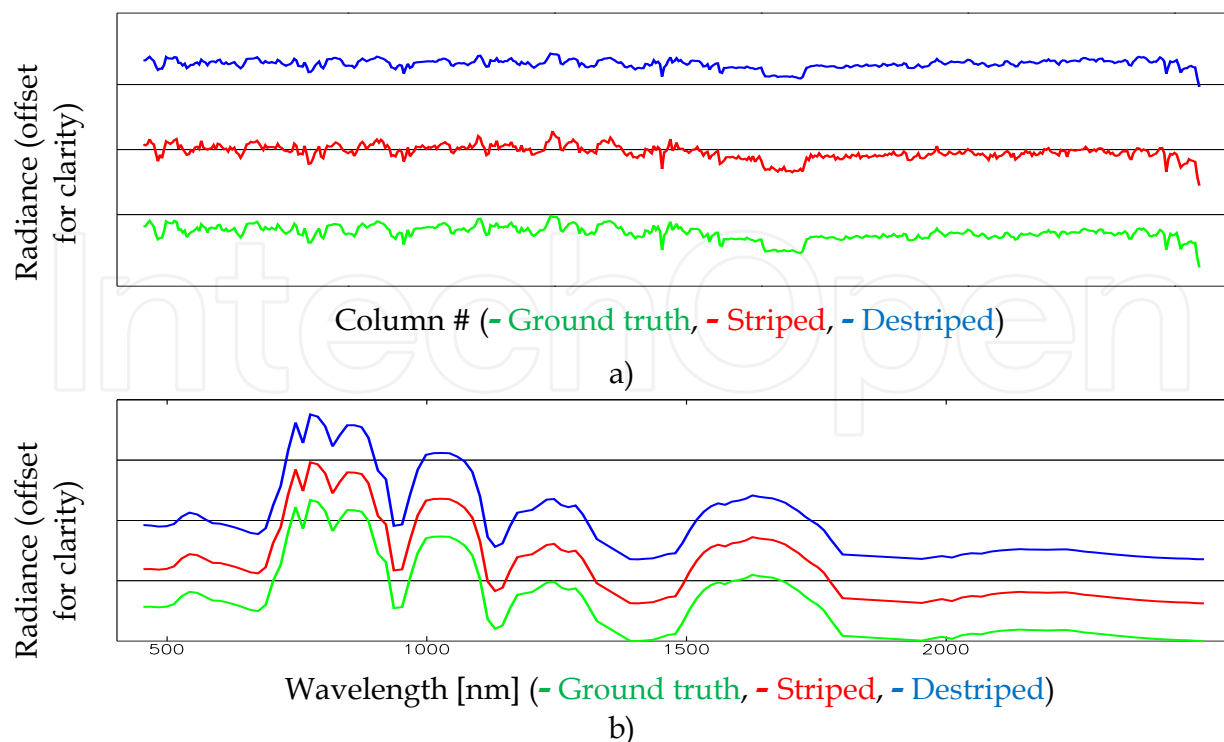


Fig. 5. Random arbitrary transect a) and spectral profile for a random point due to the subsets of Fig. 4 a), b) and c)

4.3 ASTER

The ASTER sensor was selected for destriping since it has broader bands as an typical hyperspectral sensor and the potential miscalibration is often underestimated in the literature. However, the visible and near infrared bands were selected since these bands were mostly perceptible miscalibrated as exemplarily shown in Fig. 6. With regard to the results of Tab. 1 the destriping of the ASTER scene improved the radiometric calibration by 8 % on average. That is significant in comparison to the CHRIS/Proba related destriping results. As perceptible in Fig. 6 all stripes were removed.

As shown in Fig. 6 and 7 miscalibration is mostly visually perceptible in contrary to arbitrary transects as presented in Fig. 7a). However, the ROME framework and the adaptive detrending reduced the miscalibration. In consequence, the spectral profile has changed as given in Fig. 7 b). Contrary to airborne sensors miscalibrations of satellite sensors such as ASTER slowly vary over time. It follows from this that correction sets obtained by the ROME framework can be reused for scenes that are timely close.

4.4 CHRIS/Proba

As shown in Fig. 8 the test scene acquired by the CHRIS sensor is well calibrated. However, remaining miscalibration is visually perceptible as given in Fig. 8 c).

With regard to Tab. 1 ROME improved the radiometric calibration by 1 % on average. This shows on the one hand that the scene of this sensor was well calibrated and on the other hand that ROME is also able to detect and to reduce small variations of miscalibrations.

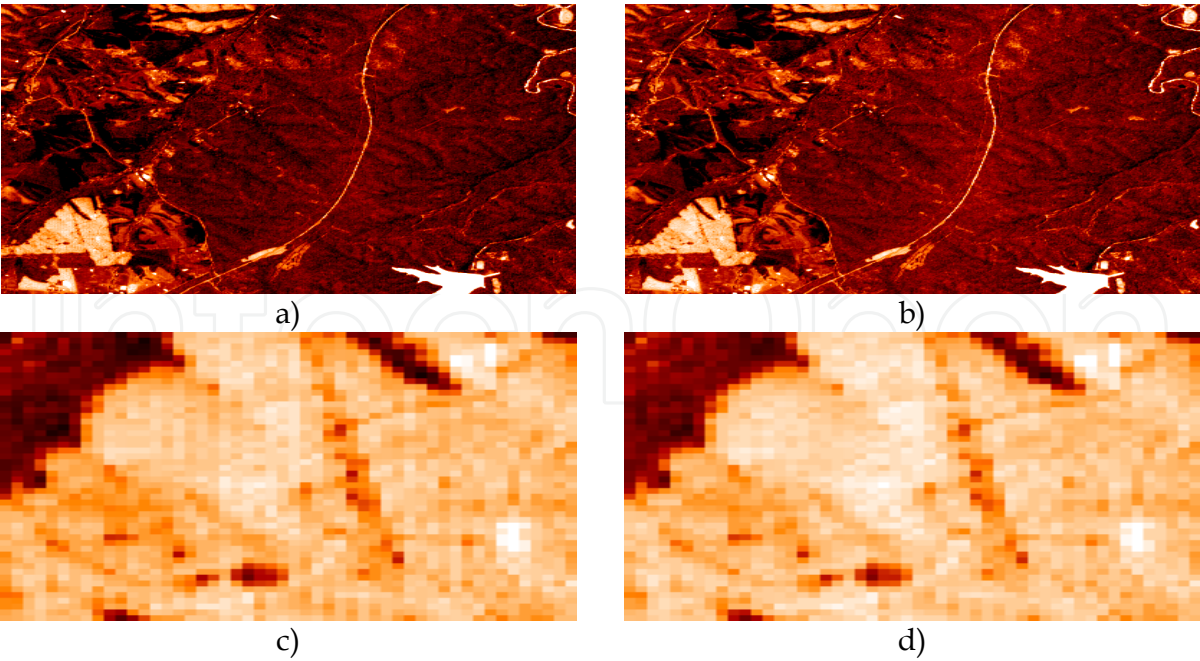


Fig. 6. False coloured image subset of band 3 (807 nm) of a striped ASTER scene (subset a and zoom c) and the ROME result adaptively detrended (subset b and zoom d)

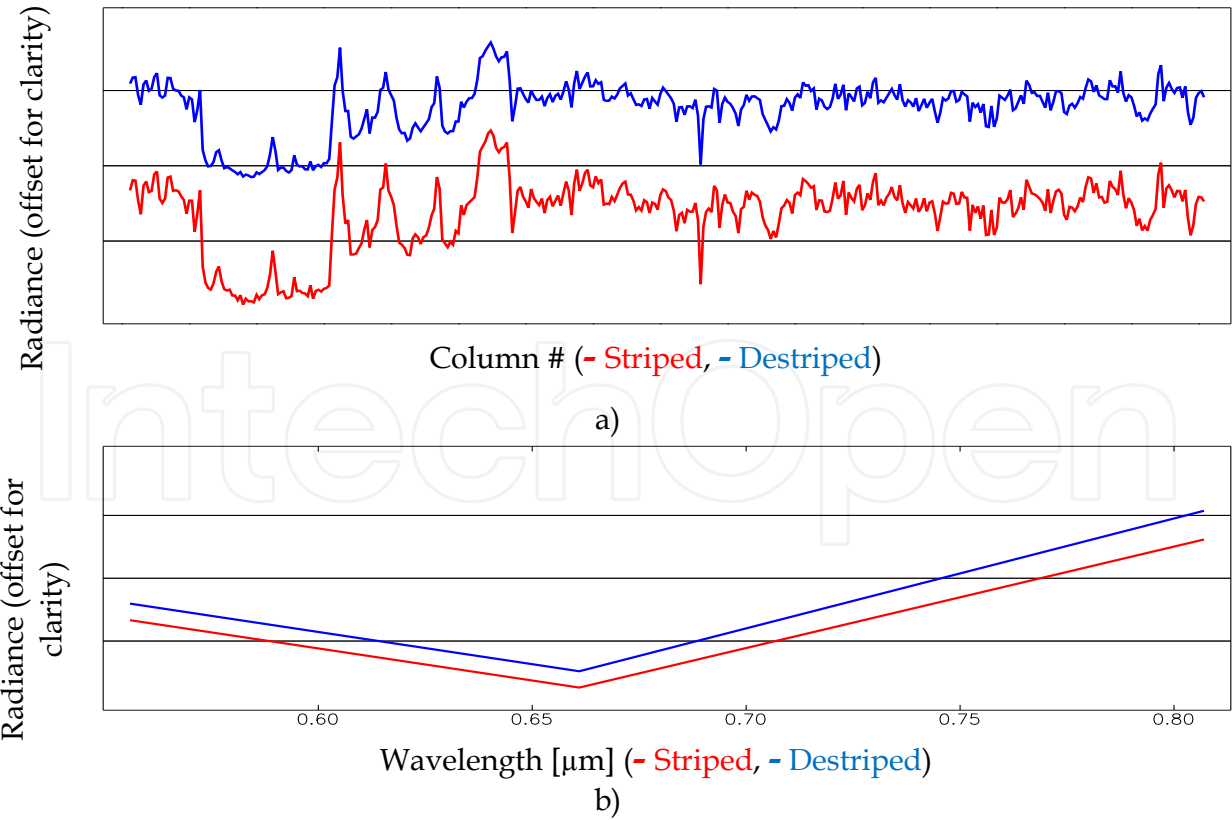


Fig. 7. Random arbitrary transect a) and spectral profile for a random point due to the subsets of Fig. 6 a) and b)

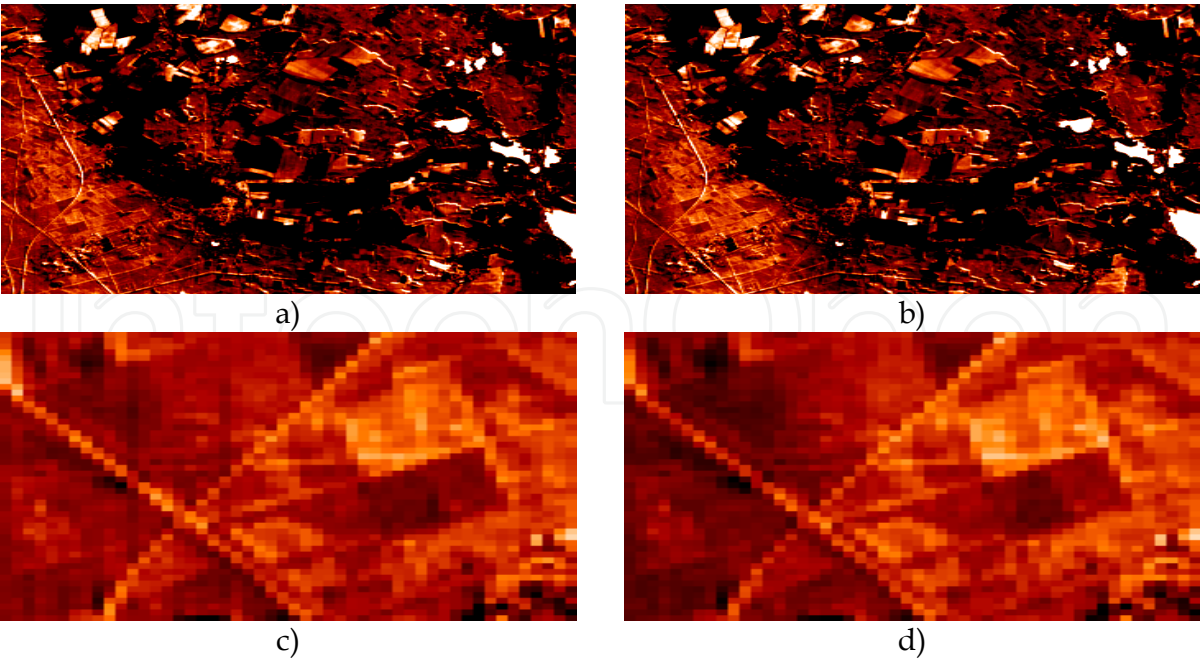


Fig. 8. False coloured image subset of band 44 (803.8 nm) of a striped CHRIS/Proba scene (subset a and zoom c) and the ROME result adaptively detrended (subset b and zoom d)

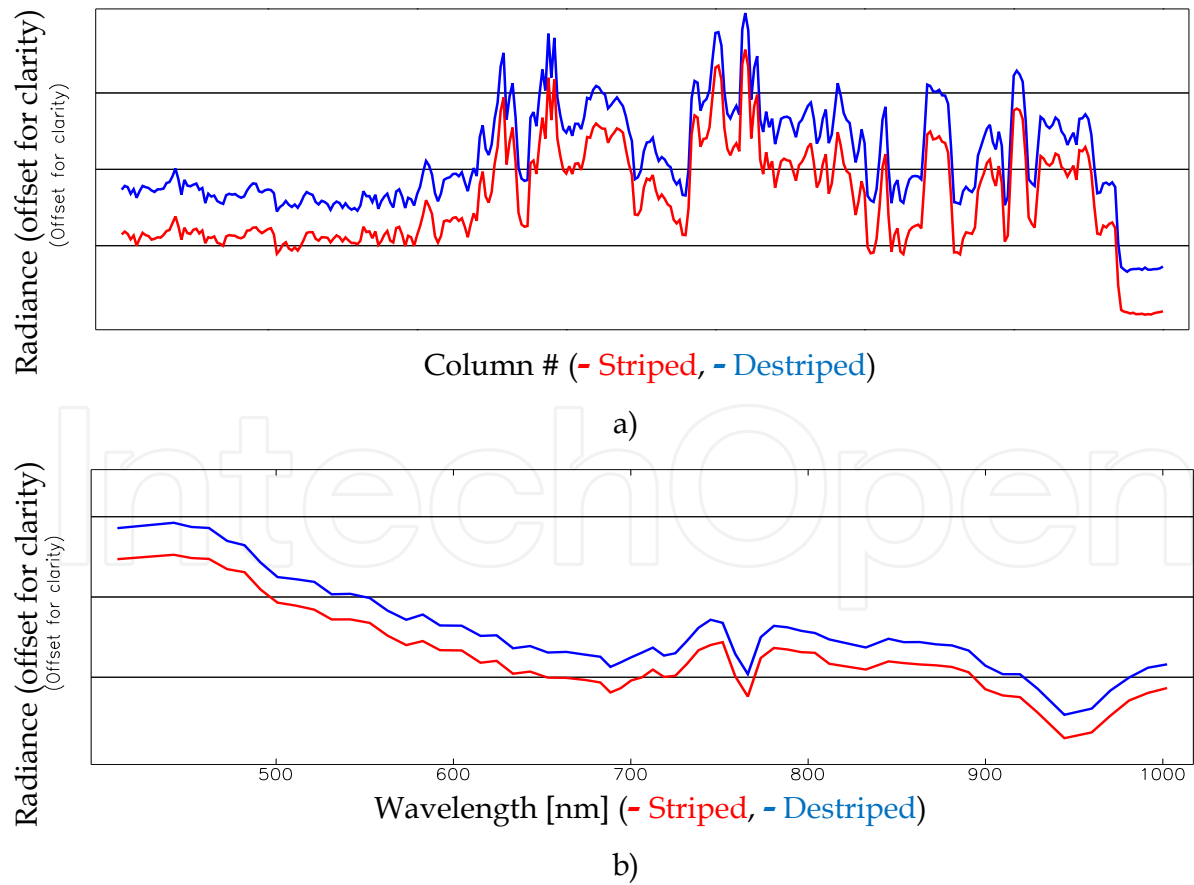


Fig. 9. Random arbitrary transect a) and spectral profile for a random point due to the subsets of Fig. 8 a) and b)

The transect as well as the spectral profile given in Fig. 9 show that ROME preserved spatial and spectral shapes. Contrary to ASTER it appears that the ROME destriping of CHRIS/Proba scenes is only necessary if succeeding processing consider adjacent image columns. In relation to Rogass et al. (2011) 97 % of a perfect calibration can be recovered by ROME. It follows from this that the decision whether ROME is applied on CHRIS/Proba or not should be application driven.

4.5 APEX

The APEX sensor belongs to the recently developed pushbroom sensors and offers a high SNR for a broad set of applications. However, as most pushbroom sensors APEX acquisitions also show perceptible variations in dark current as offset stripes although it is well calibrated like CHRIS/Proba. These stripes are difficult to be detected due to the high SNR of APEX and to the overall low contribution of miscalibration to image spectra. To additionally test the new detrending approach, a subset of a scene (400 lines) was used. In consequence, the results of Tab. 1 that show an overall improvement of calibration of about 8 % are not fully representative for the APEX sensor. In this case it is assumed that 97 % of a perfect calibration has been achieved. The respective results are exemplarily represented in Fig. 10 and 11. Comparing the along track transect of Fig. 11 a) and the spectral profile of Fig. 11 b) with the false coloured image representations of Fig. 10 it appears that changes of spectra are mostly visually perceptible. That supports the assumption that APEX acquisitions are not dominated by dark current variations contrary to Hyperion or AISA DUAL. The assumption that potential frequency undershoots caused by, e.g. offset reductions, are minimised by the new detrending approach is also supported (compare also next chapter).

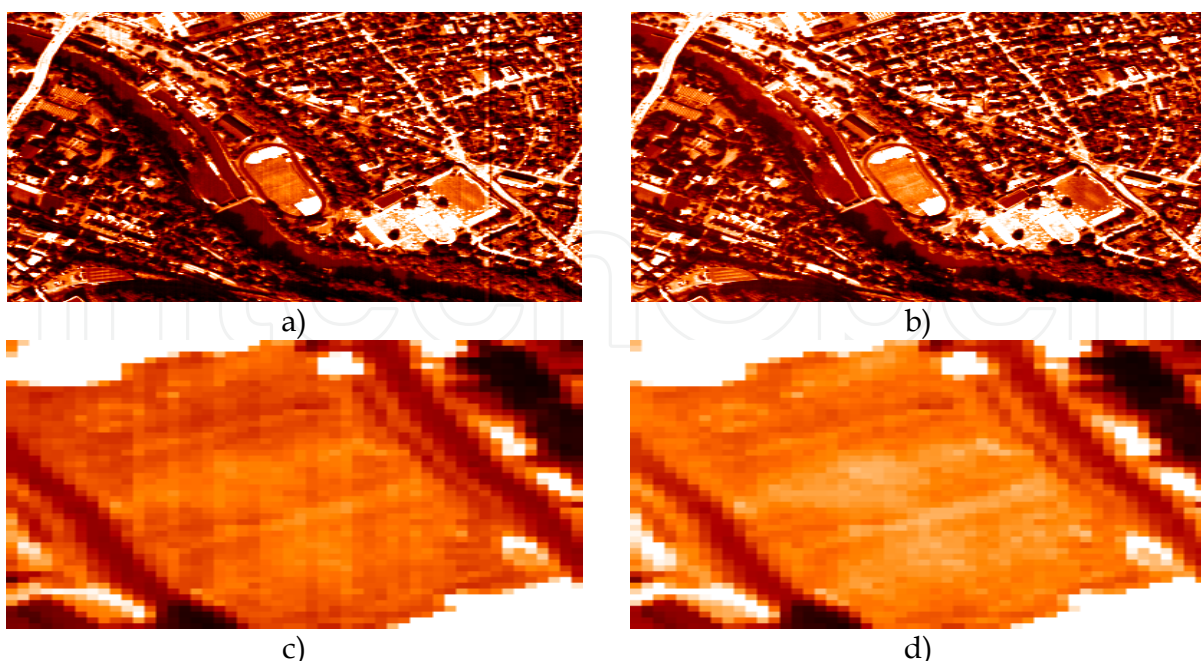


Fig. 10. False coloured image subset of band 19 (557.3 nm) of a striped APEX scene (subset a and zoom c) and the ROME result adaptively detrended (subset b and zoom d)

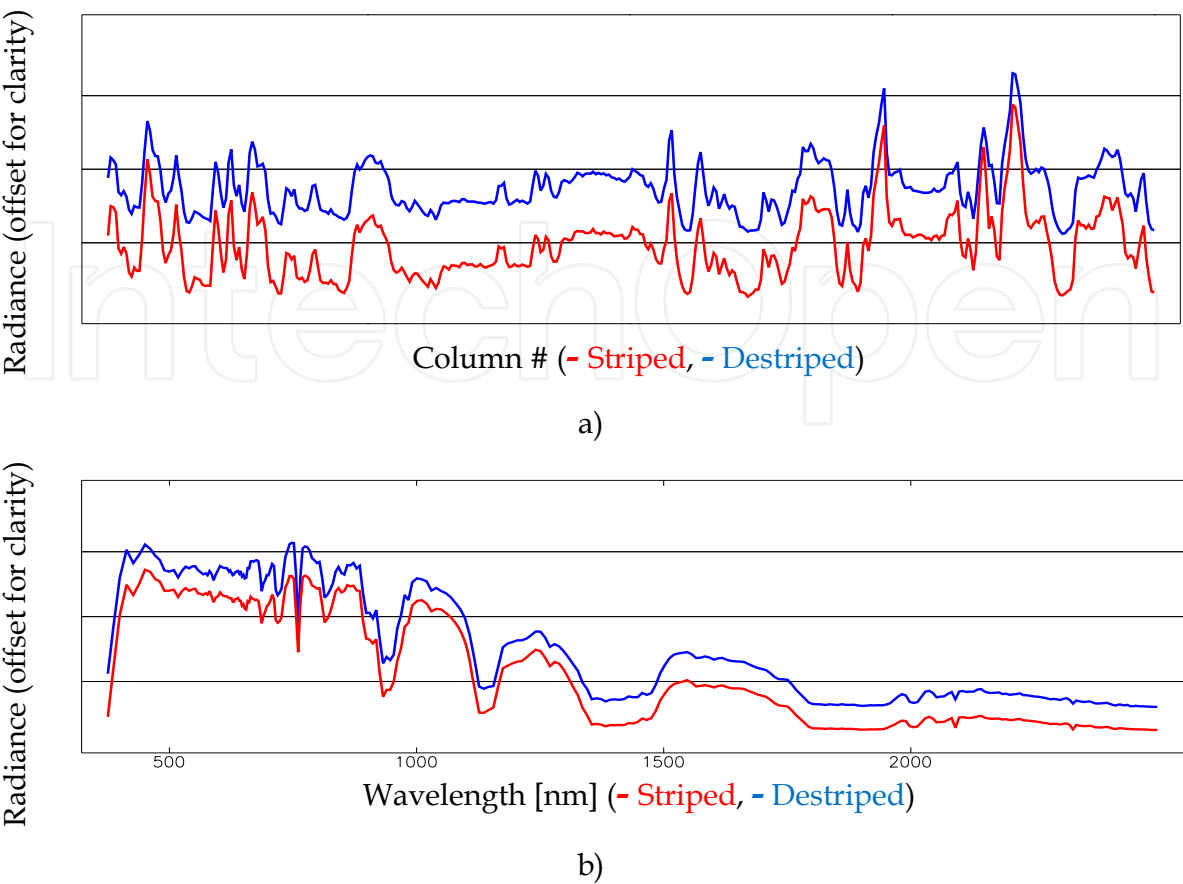
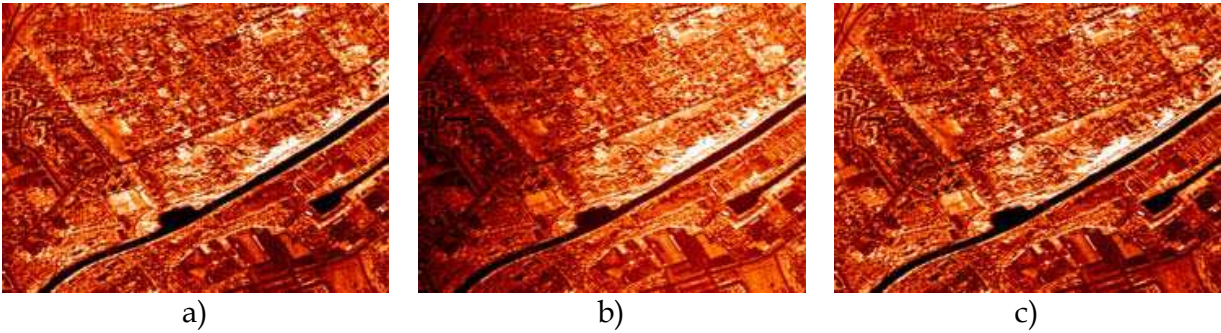


Fig. 11. Random arbitrary transect a) and spectral profile for a random point due to the subsets of Fig. 10 a) and b)

4.6 Results for extended detrending

The ROME framework as proposed in Rogass et al. (2011) has limited facilities for short scenes. In this work the impact of short scenes is inspected and an extension to its detrending proposed. Since the effect varies from scene to scene and sensor to sensor it is not possible to quantify the impact. To qualify the impact of short scenes on ROME, one artificially offset striped HyMAP scene subset (SNR=7.6) was destriped. Then, the result was ROME detrended and detrended by the nex approach. The respective results are given Fig. 12 and 13. As perceptible in Fig. 12 b) and e) compared to Fig. 12 c and f significant reduction related brightness gradients are significantly reduced by the new approach.



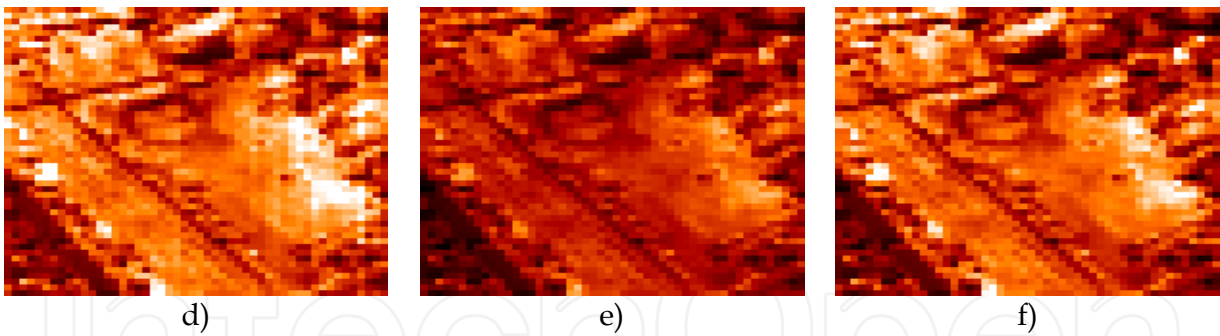


Fig. 12. False coloured, small image subset of band 30 (874 nm) of a HyMAP scene (subset a and zoom d) that war artificially offset striped (SNR=7.6), ROME result (subset b and zoom e) and the ROME result adaptively detrended (subset c and zoom f)

The across track transect as well as the spectral profile given in Fig. 13 clearly show the impact of the detrending on the spectral scale. Comparing the old detrending approach with the new detrending approach leads to the perception that the new detrending preserves the spectral profile in both directions the spatial domain - across track (correction direction) and the spectral domain - along the spectrum.

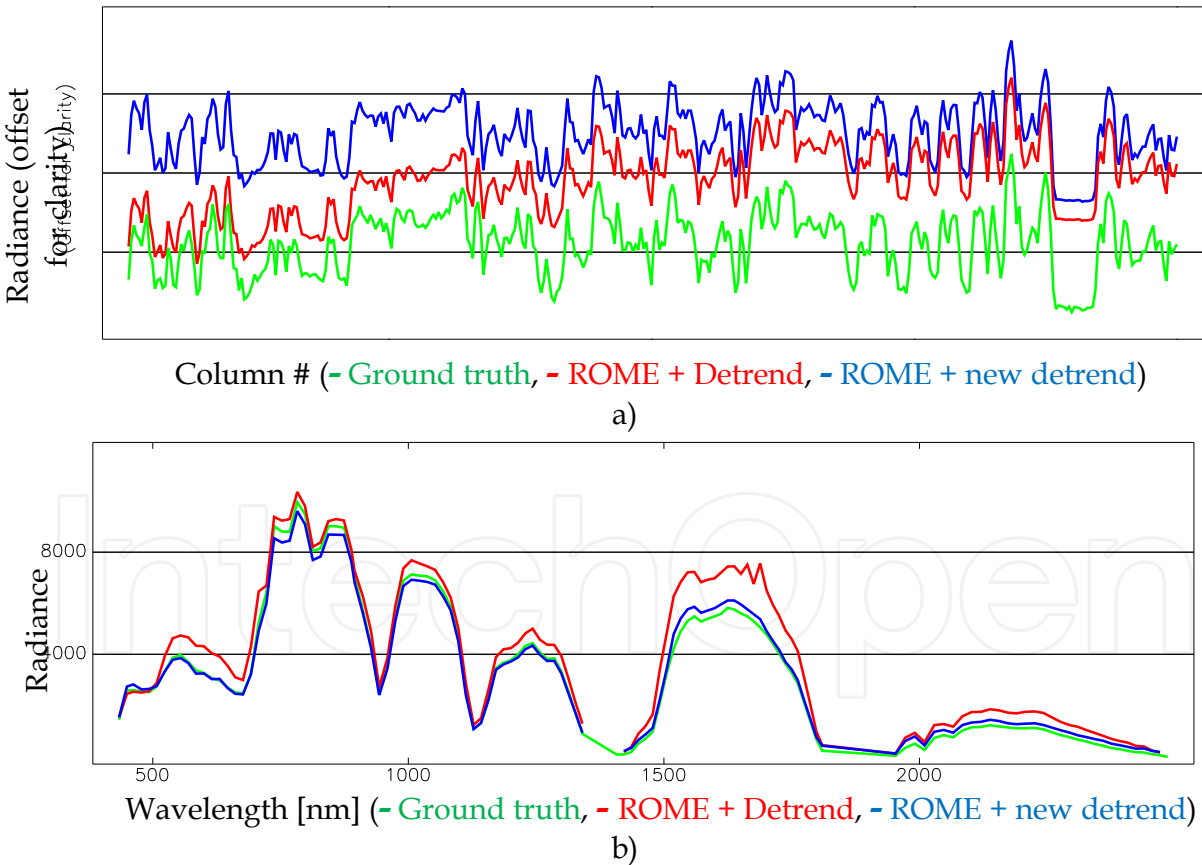


Fig. 13. Random arbitrary transect a) and spectral profile for a random point due to the subsets of Fig. 10 a) and b)

It follows from this that relatively short scenes are more difficult to correct as long scenes. In Rogass et al. (2011) it was assumed that the ROME correction facilities are dependent on the

along track dimension. This is supported and can be clearly demonstrated, e.g. by transects and spectral profiles of corrected short scenes as presented in Fig. 12 and 13. The subsets for detrending comparisons had a size of 400 lines.

5. Conclusions

Pushbroom sensors must be carefully calibrated and miscalibrations aggravate succeeding operations such as atmospheric correction (Richter, 1997), classification and segmentation (Datt et al., 2003). Therefore, it is necessary to efficiently reduce them. The ROME framework and the extended detrending proposed in this work significantly reduce miscalibrations of any type. Like other methods there are also limitations. These limitations mostly relate to offset and nonlinear reductions, not the linear slope reduction.

However, a calibration recovery rate of about 97 % still remains uncertainties. High spatial densities of translucent objects such as trees reduce offset reduction facilities and should be excluded beforehand. Tests with different data sets also showed that dense haze or clouds may hinder offset reduction. These effects can be minimised by destriping subsets and by applying estimated correction coefficients on the whole image. In case of clouds or dense haze a reference column for offset reduction that is haze or cloud free is suggested.

With regard to tests of Rogass et al. (2011) and tests performed for this work it can be assumed that the ROME framework is capable to reduce miscalibrations for most pushbroom sensors. With regard to the high processing speed and the freedom of parameters it can be operationally used. The nonlinear correction has to be improved but represents the current state of the art method as the other methods implemented in ROME. However, further research is necessary. This is particularly applicable for high frequency undershoots that are currently not considered.

6. References

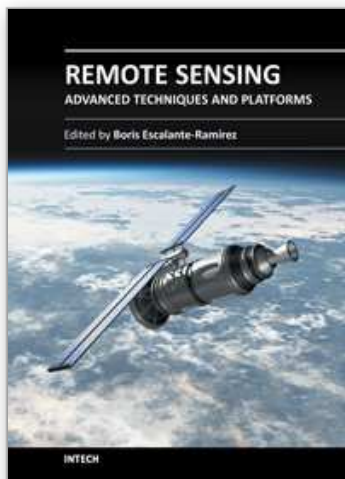
- Atkinson, P.M.; Sargent, I.M.; Foody, G.M.; Williams, J. Interpreting Image-Based Methods for Estimating the Signal-to-Noise Ratio. *Int. J. Rem. Sens.* 2005, 26, 5099–5115.
- Barducci, A.; Castagnoli, F.; Guzzi, D.; Marcoionni, P.; Pippi, I.; Poggesi, M. Solar Spectral Irradiometer for Validation of Remotely Sensed Hyperspectral Data. *Appl. Opt.* 2004, 43, 183–195.
- Barnsley, M. J., Allison, D., Lewis, P. 1997. On the information content of multiple view angle (MVA) images. *International Journal of Remote Sensing*, 18:1936– 1960.
- Biggar, S.; Thome, K.; Wisniewski, W. Vicarious Radiometric Calibration of EO-1 Sensors by Reference to High-Reflectance Ground Targets. *IEEE Trans. Geosci. Rem. Sens.* 2003, 41, 1174–1179.
- Bindschadler, R.; Choi, H. Characterizing and Correcting Hyperion Detectors Using Ice-Sheet Images. *IEEE Trans. Geosci. Rem. Sens.* 2003, 41, 1189–1193.
- Bouali, M.; Ladjal, S. A Variational Approach for the Destriping of Modis Data. In *IGARSS 2010: Proceedings of the IEEE International Geoscience and Remote Sensing Symposium*, Honolulu, Hawaii, 25–30 July, 2010; pp. 2194–2197.
- Box, G.; Muller, M. A Note on the Generation of Random Normal Deviates. *Ann. Math. Stat.* 1958, 29, 610–611.

- Bruegge, C.; Diner, D.; Kahn, R.; Chrien, N.; Helmlinger, M.; Gaitley, B.; Abdou, W. The Misr Radiometric Calibration Process. *Rem. Sens. Environ.* 2007, 107, 2–11.
- Brunn, A.; Fischer, C.; Dittmann, C.; Richter, R. Quality Assessment, Atmospheric and Geometric Correction of Airborne Hyperspectral Hymap Data. In *Proceedings of the 3rd EARSeL Workshop on Imaging Spectroscopy*, Herrsching, Germany, 13–16 May 2003; pp. 72–81.
- Canny, J. A Computational Approach to Edge Detection. *IEEE Trans. Pattern Anal. Mach. Intell.* 1986, 8, 679–698.
- Carfantan, H.; Idier, J. Statistical linear destriping of satellite-based pushbroom-type images. *IEEE Trans. Geosci. Rem. Sens.* 2010, 48, 1860–1871.
- Cavalli, R.; Fusilli, L.; Pascucci, S.; Pignatti, S.; Santini, F. Hyperspectral Sensor Data Capability for Retrieving Complex Urban Land Cover in Comparison with Multispectral Data: Venice City Case Study (Italy). *Sensors* 2008, 8, 3299–3320.
- Chander, G.; Markham, B.; Helder, D. Summary of Current Radiometric Calibration Coefficients for Landsat MSS, TM, ETM+, and EO-1 ALI Sensors. *Rem. Sens. Environ.* 2009, 113, 893–903.
- Cocks, T., Jenssen, R., Stewart, A., Wilson, I., and Shields, T., 1998, The HyMap airborne hyperspectral sensor: the system, calibration and performance, First EARSeL Workshop on Imaging Spectroscopy, 6–8 Oct. 1998, Zurich, Switzerland, pp. 37–42.
- Datt, B.; McVicar, T.R.; van Niel, T.G.; Jupp, D.L.B.; Pearlman, J.S. Preprocessing EO-1 Hyperion Hyperspectral Data to Support the Application of Agricultural Indexes. *IEEE Trans. Geosci. Rem. Sens.* 2003, 41, 1246–1259.
- Dell'Endice, F. Improving the Performance of Hyperspectral Pushbroom Imaging Spectrometers for Specific Science Applications. In *ISPRS 2008: Proceedings of the XXI Congress: Silk Road for Information from Imagery: The International Society for Photogrammetry and Remote Sensing*, 3–11 July, Beijing, China, 2008; pp. 215–220.
- Dell'Endice, F.; Nieke, J.; Koetz, B.; Schaepman, M.E.; Itten, K. Improving Radiometry of Imaging Spectrometers by Using Programmable Spectral Regions of Interest. *ISPRS J. Photogramm. Rem. Sens.* 2009, 64, 632–639.
- Frank, S.; Smith, E. Measurement Invariance, Entropy, and Probability. *Entropy* 2010, 12, 289–303.
- Gao, B.-C. An Operational Method for Estimating Signal to Noise Ratios from Data Acquired with Imaging Spectrometers. *Rem. Sens. Environ.* 1993, 43, 23–33.
- García, J.; Moreno, J. Removal of Noises in CHRIS/Proba Images: Application to the SPARC Campaign Data. In *Proceedings of the 2nd CHRIS/Proba Workshop*, ESA/ERSIN, Frascati, Italy, 28–30 April, 2004; pp. 29–33.
- Gómez-Chova, L.; Alonso, L.; Guanter, L.; Camps-Valls, G.; Calpe, J.; Moreno, J. Correction of Systematic Spatial Noise in Push-Broom Hyperspectral Sensors: Application to CHRIS/Proba Images. *Appl. Opt.* 2008, 47, F46–F60.
- Guanter, L.; Segl, K.; Kaufmann, H. Simulation of optical remote-sensing scenes with application to the enmap hyperspectral mission. *IEEE Trans. Geosci. Rem. Sens.* 2009, 47, 2340–2351.
- Haralick, R.M.; Sternberg, S.R.; Zhuang, X. Image Analysis Using Mathematical Morphology. *IEEE Trans. Pattern Anal. Mach. Intell.* 1987, 9, 532–550.

- Itten, K. I.; Dell'Endice, F.; Hueni, A.; Kneubühler, M.; Schläpfer, D.; Odermatt, D.; Seidel, F.; Huber, S.; Schopfer, J.; Kellenberger, T.; Bühler, Y.; D'Odorico, P.; Nieke, J.; Alberti, E.; Meuleman, K. APEX - the Hyperspectral ESA Airborne Prism Experiment. *Sensors* 2008, 8, 6235-6259.
- Kaufmann, H.; Segl, K.; Guanter, L.; Förster, K.P.; Stuffer, T.; Müller, A.; Richter, R.; Bach, H.; Hostert, P.; Chlebek, C. Environmental Mapping and Analysis Program (EnMAP) – Recent Advances and Status. In *IGARSS 2008: Proceedings of the IEEE International Geoscience and remote Sensing Symposium*, 7-11 July, Boston, MA, USA, 2008; pp. IV-109-IV-112.
- Le Maire, G.; François, C.; Soudani, K.; Berveiller, D.; Pontailier, J.-Y.; Bréda, N.; Genet, H.; Davi, H.; Dufrêne, E. Calibration and Validation of Hyperspectral Indices for the Estimation of Broadleaved Forest Leaf Chlorophyll Content, Leaf Mass Per Area, Leaf Area Index and Leaf Canopy Biomass. *Rem. Sens. Environ.* 2008, 112, 3846-3864.
- Liu, B.; Zhang, L.; Zhang, X.; Zhang, B.; Tong, Q. Simulation of EO-1 Hyperion Data from ALI Multispectral Data Based on the Spectral Reconstruction Approach. *Sensors* 2009, 9, 3090-3108.
- Oliveira, P.; Gomes, L. Interpolation of Signals with Missing Data Using Principal Component Analysis. *Multidimens. Syst. Signal Process.* 2010, 21, 25-43.
- Oppelt, N.; Mauser, W. The Airborne Visible/Infrared Imaging Spectrometer Avis: Design, Characterization and Calibration. *Sensors* 2007, 7, 1934-1953.
- Richter, R. Correction of Atmospheric and Topographic Effects for High Spatial Resolution Satellite Imagery. *Int. J. Rem. Sens.* 1997, 18, 1099-1111.
- Rogass, C.; Itzerott, S.; Schneider, B.; Kaufmann, H.; Hüttel, R. Edge Segmentation by Alternating Vector Field Convolution Snakes. *Int. J. Comput. Sci. Netw. Secur.* 2009, 9, 123-131.
- Rogass, C.; Itzerott, S.; Schneider, B.; Kaufmann, H.; Hüttel, R. Hyperspectral Boundary Detection Based on the Busyness Multiple Correlation Edge Detector and Alternating Vector Field Convolution Snakes. *ISPRS J. Photogramm. Rem. Sens.* 2010, 55, 468-478.
- Rogass, C.; Spengler, D.; Bochow, M.; Segl, K.; Lausch, A.; Doktor, D.; Roessner, S.; Behling, R.; Wetzel, H.-U.; Kaufmann, H. Reduction of Radiometric Miscalibration – Applications to Pushbroom Sensors. *Sensors* 2011, 11, 6370-6395.
- Segl, K.; Guanter, L.; Kaufmann, H.; Schubert, J.; Kaiser, S.; Sang, B.; Hofer, S. Simulation of Spatial Sensor Characteristics in the Context of the EnMAP Hyperspectral Mission. *IEEE Trans. Geosci. Rem. Sens.* 2010, 48, 3046-3054.
- Shen, H.F.; Ai, T.H.; Li, P.X. Destriping and Inpainting of Remote Sensing Images Using Maximum a-Posteriori Method. In *ISPRS 2008: Proceedings of the XXI Congress: Silk Road for Information from Imagery: The International Society for Photogrammetry and Remote Sensing*, 3-11 July, Beijing, China, 2008; pp. 63-70.
- Simpson, J.J.; Gobat, J.I.; Frouin, R. Improved Destriping of Goes Images Using Finite Impulse Response Filters. *Rem. Sens. Environ.* 1995, 52, 15-35.
- Simpson, J.J.; Stitt, J.R.; Leath, D.M. Improved Finite Impulse Response Filters for Enhanced Destriping of Geostationary Satellite Data. *Rem. Sens. Environ.* 1998, 66, 235-249.
- Spectral Imaging Ltd. Aisa Dual, 2nd Version. Available online: http://www.specim.fi/media/aisa-datasheets/dual_datasheet_ver2-10.pdf (accessed on 5 January 2011).

- Tsai, F.; Chen, W. Striping Noise Detection and Correction of Remote Sensing Images. *IEEE Trans. Geosci. Rem. Sens.* 2008, 46, 4122–4131.
- Ungar, S.G.; Pearlman, J.S.; Mendenhall, J.A.; Reuter, D. Overview of the Earth Observing One (EO-1) Mission. *IEEE Trans. Geosci. Rem. Sens.* 2003, 41, 1149–1159.
- Wang, Z.; Bovik, A.C. Mean Squared Error: Love It or Leave It? A New Look at Signal Fidelity Measures. *IEEE Signal Process. Mag.* 2009, 26, 98–117.
- Wang, Z.; Bovik, A.C.; Sheikh, H.R.; Simoncelli, E.P. Image Quality Assessment: From Error Visibility to Structural Similarity. *IEEE Trans. Image Process.* 2004, 13, 600–612.
- Weber, A. The USC-SIPI Image Database; Technical Report, University of Southern California, Signal and Image Processing Institute: Los Angeles, CA, USA, 1997.
- Xiong, X.; Barnes, W. An Overview of Modis Radiometric Calibration and Characterization. *Adv. Atmos. Sci.* 2006, 23, 69–79.
- Yamaguchi, Y.; Kahle, A.B.; Tsu, H.; Kawakami, T.; Pniel, M. Overview of Advanced Spaceborne Thermal Emission and Reflection Radiometer (ASTER). *IEEE Trans. Geosci. Remote Sensing* 1998, 36(4), 1062–1071.

IntechOpen



Remote Sensing - Advanced Techniques and Platforms

Edited by Dr. Boris Escalante

ISBN 978-953-51-0652-4

Hard cover, 462 pages

Publisher InTech

Published online 13, June, 2012

Published in print edition June, 2012

This dual conception of remote sensing brought us to the idea of preparing two different books; in addition to the first book which displays recent advances in remote sensing applications, this book is devoted to new techniques for data processing, sensors and platforms. We do not intend this book to cover all aspects of remote sensing techniques and platforms, since it would be an impossible task for a single volume. Instead, we have collected a number of high-quality, original and representative contributions in those areas.

How to reference

In order to correctly reference this scholarly work, feel free to copy and paste the following:

Christian Rogaß, Daniel Spengler, Mathias Bochow, Karl Segl, Angela Lausch, Daniel Doktor, Sigrid Roessner, Robert Behling, Hans-Ulrich Wetzels, Katia Urata, Andreas Hueni and Hermann Kaufmann (2012). A Contribution to the Reduction of Radiometric Miscalibration of Pushbroom Sensors, Remote Sensing - Advanced Techniques and Platforms, Dr. Boris Escalante (Ed.), ISBN: 978-953-51-0652-4, InTech, Available from: <http://www.intechopen.com/books/remote-sensing-advanced-techniques-and-platforms/a-contribution-to-the-reduction-of-radiometric-miscalibration-of-pushbroom-sensors>

INTECH
open science | open minds

InTech Europe

University Campus STeP Ri
Slavka Krautzeka 83/A
51000 Rijeka, Croatia
Phone: +385 (51) 770 447
Fax: +385 (51) 686 166
www.intechopen.com

InTech China

Unit 405, Office Block, Hotel Equatorial Shanghai
No.65, Yan An Road (West), Shanghai, 200040, China
中国上海市延安西路65号上海国际贵都大饭店办公楼405单元
Phone: +86-21-62489820
Fax: +86-21-62489821

© 2012 The Author(s). Licensee IntechOpen. This is an open access article distributed under the terms of the [Creative Commons Attribution 3.0 License](https://creativecommons.org/licenses/by/3.0/), which permits unrestricted use, distribution, and reproduction in any medium, provided the original work is properly cited.

IntechOpen

IntechOpen